

Relationship Between Inoculants and the Morphologies of MnS and Graphite in Gray Cast Iron

H.M. MUHMOND and H. FREDRIKSSON

The influence of oxides and sulfides in gray cast iron on the growth morphologies of MnS and on the nucleation of graphite was experimentally investigated using scanning electron microscopy and energy-dispersive X-ray spectroscopy (SEM-EDX) analysis with evidences that shows the possible nucleation sites for graphite nucleation. Thermodynamic studies have been done on the influence of varying sulfur concentrations on the nucleation of MnS in the melt and during solidification. The consumption of dissolved oxygen and sulfur in the melt during the cooling process was analyzed and we explored how this influenced the nucleation process of oxides and sulfides. A sequential nucleation concept of oxides and MnS is proposed in relation to the growth morphology of MnS and graphite with respect to the mechanical properties of cast iron. The nucleation of new oxides and sulfides was analyzed using thermodynamics and compared to our experimental results. Graphite nucleation on substrates other than MnS, such as MoS₂ oxides and (Mo,Cr)S, was experimentally analyzed along with the influence of the substrates on graphite nucleation and growth morphology.

DOI: 10.1007/s11663-012-9768-6

© The Minerals, Metals & Materials Society and ASM International 2012

I. INTRODUCTION

THE nucleation of graphite in cast iron has been researched for many decades and, consequently, many theories regarding graphite nucleation have been proposed. Warrick^[1] suggested that complex oxides and sulfides serve as the nuclei for flake graphite. Many other researchers came to similar conclusions, including Muzmudar *et al.*,^[2,3] Jacobs *et al.*,^[4] and Gadd *et al.*^[5] Kusakawa *et al.*^[6] have reported the presence of non-metallic inclusions that exhibited the highest inoculation effect. Campbell^[7] introduced the concept of a silica-rich oxide bifilm that nucleates on oxysulfide particles in the melt.

To precipitate graphite as a stable iron graphite eutectic structure, inoculants are added to the melt that typically consist of rare earth metals or strong deoxidizers such as Sr and Al. These inoculants produce heterogeneities in the form of oxides and sulfides to enhance the nucleation of graphite on oxysulfide particles. Each type of inoculant influences the graphitizing efficiency differently, as discussed by Riposan *et al.*^[8]; for example, Sr has a higher graphitizing efficiency than Ba and Ca. Researchers have found that the (Mn,X)S particle (X = Al, Sr, Ca, ...) acts as a nucleation site for graphite.^[9–12] Velichko *et al.*^[13] performed a 3D visualization of the eutectic cell and found many small MnS inclusions within a thick graphite flake. Skaland^[14] proposed a mathematical model for the heterogeneous

nucleation of graphite in cast iron based on the concept of interfacial energies and lattice disregistry. According to Skaland, undercooling decreases in a parabolic manner with increasing values of the planner lattice disregistry. Hua Qu *et al.*^[15] analyzed the lattice structure of graphite and compared it to those of CaS and MnS. Hua Qu found a close match between the lattice parameters of MnS and CaS and those of graphite. Sommerfeld *et al.*^[16] concluded that Mn/S ratio influences graphite nucleation. Similarly, the content of Mn in cast iron has been investigated many times by different researchers, whereby the ratio of Mn/S was explored with respect to the graphite precipitation process and morphology along with its relationship to the tensile strength of cast iron (Muzmudar *et al.*,^[2] Goodrich *et al.*,^[17] Sommerfeld *et al.*^[16] and Fras *et al.*^[18]).

The role of MnS with a varying sulfur concentration in the alloy, the nucleation of oxides in the melt due to inoculation, and the influence of MnS and oxides on the growth morphology of graphite were investigated experimentally and by thermodynamic analysis. The samples were analyzed by energy-dispersive X-ray spectroscopy (EDX) to verify different types of oxide/sulfide inclusions formed during inoculation. One of our goals was to observe the morphological differences in graphite and MnS with respect to inoculation.

II. EXPERIMENTAL PROCEDURE

A. Materials

One cast iron base was used and from this base iron, several other cast iron alloys were prepared in the quartz crucible, while varying the S content by adding pure Ca

H. M. MUHMOND, Ph.D student, and H. FREDRIKSSON, Professor, are with the Materials Science and Engineering Department, Royal Institute of Technology, Brinellvägen 23, 10044, Stockholm, Sweden. Contact e-mail: haji@kth.se

Manuscript submitted May 26, 2012.

Article published online December 18, 2012.

as a desulfurizer and a calculated amount of C to compensate for its loss (Table I). Two more alloys were prepared in alumina crucible by adding C, Si, and all other alloys into pure iron melt; however, Mn was excluded (Table I). The alloys composition was determined using spark emission spectroscopy. A high-frequency (HF) induction furnace was used to melt the alloys in a high-grade transparent quartz tube surrounded by a graphite susceptor. The settings of the HF induction furnace were chosen such that the maximum temperature of the melt ranged from 1573 to 1623 K (1300 to 1350 °C). The samples were melted under argon atmosphere. The temperature was monitored from the wall of the quartz tube, in center of the melt, using an infrared pyrometer (with an uncertainty of 0.4 pct of T), which was calibrated for each experiment to the melting point of the alloy. Commercially available Superseed[®] inoculant, which contains 75.5 wt pct Si, 0.5 wt pct Al, 0.1 wt pct Ca, and 1.1 wt pct Sr and Fe balance, was used in most of the experiments.

B. Experiments

Five different experimental series were investigated. In the first series (ES1-1 to ES1-9), the samples were melted and heated to approximately 1623 K (1350 °C). The melt was inoculated in the quartz tube, cooled to a defined temperature, and quenched (except ES1-7) by dropping the quartz tube into a 10 pct brine solution containing crushed ice (Table II). Quenching experiments were performed to determine what types of inclusions were formed at a certain temperature. The dimensions of the quartz tubes were (in mm) ID 5, OD 7; ID 7.3, OD 10.3; and ID 12.5, OD 15 for experiments ES1(8,9), ES1(1-5), and ES1(6,7), respectively (Table II). In the second (ES2), third (ES3), and fourth (ES4) series, all samples were cooled in the crucible (quartz tube of ID = 12.5 mm, OD = 15 mm) to room temperature (Table III). A cooling rate of approximately 60 K (°C)/min was achieved by wrapping a thick insulating material around the crucible and inserting it into a (relatively) large quartz tube. The final series of experiments was performed in a differential scanning calorimeter (DSC-404, calibrated to pure metals) under argon atmosphere at a stable, controlled cooling rate of 15 K (°C)/min from 1573 K (1300 °C) to room temperature for each sample. These DSC experiments allowed us to solidify the alloy at a lower cooling rate to

carefully examine the precipitation of MnS in the melt and during solidification (Table IV).

C. Microstructural Analysis

An optical microscope and scanning electron microscope (SEM S-3700N) were used for microstructure analysis. X-ray microanalysis of the inclusions was carried out using EDX, all with proper accelerating voltages according to the size of the measuring particle to obtain the desired analysis volume. For smaller size particles ($\leq 1 \mu\text{m}$), the secondary electron (SE) source was used with an acceleration voltage (AC) of 10 kV and an emission current of 35–39 μA , but for large size inclusions, an AC 15 to 20 kV was used. The measurements were normalized to 100 pct after considering all the possible elements present according to the composition of the alloy.

III. RESULTS

A. EDX Analysis

The EDX analysis was divided into three parts based on the formation of oxides in different sulfur-containing alloys, the formation of nitrides, and the formation of Mo-containing complex particles (Tables II, III). The analysis were performed along the direction and length of the arrows that are shown in the thumbnail images in Figure 1. Each analysis consisted of 20 to 30 data points along the arrow line, as shown graphically in Figure 1.

All MnS particles contained some amount of Mo, which could be interpreted as a compound of (Mn,Mo)S from the EDX profile. The dark portion in the SEM images (Figures 1(a) through (d), (g), (h)) is graphite. Aluminum oxide was found in most of the particles, situated in the core of the particles surrounded by MnS (Figures 1(a) through (c)). Other oxides such as SrO, CaO/S, and SiO₂ were found in the core of the particles, surrounded by MnS or (Mn,Mo)S connected with graphite. The size of MnS inclusions decreased with decreasing sulfur content in the alloy as a result of the late nucleation of MnS on oxides, while the Mo content is constant (Figures 1(a) through (c)). In the sample of sulfur content 0.007 wt pct, Mo formed a complex compound with Ca as (Mo,Ca)S together with Al₂O₃ and graphite (Figure 1(c)). From the microstructure

Table I. Composition of the Alloys in Weight Percentage

Alloy	C	Si	Mn	S	Mo	Cr	N	P	Ti	Cu	C.E
S0.107	3.41	1.93	0.61	0.107	0.22	0.26	0.006	0.022	0.009	0.56	4.05
S0.061	3.45	1.97	0.65	0.061	0.22	0.27	0.006	0.028	0.01	0.59	4.1
S0.028	3.47	1.96	0.58	0.028	0.21	0.26	0.002	0.028	0.009	0.6	4.12
S0.021	3.44	1.93	0.64	0.021	0.22	0.26	0.003	0.026	0.009	0.59	4.08
S0.010	3.41	1.98	0.58	0.01	0.2	0.26	0.003	0.027	0.009	0.6	4.07
S0.007	3.41	1.92	0.63	0.007	0.22	0.27	0.001	0.025	0.009	0.59	4.05
L-Mn	3.22	2.37	0.04	0.013	0.13	0.28	0.016	0.002	0.005	0.69	4.01
N-Mn	3.32	2.04	0	0.094	0.12	0.25	0.002	0.001	0.001	0.66	4

S, sulfur; N-Mn, no manganese; L-Mn, low manganese; C.E, carbon equivalent (pct C + (pct Si/3)).

Table II. Samples Quenched in Brine After Inoculation (Except Sample ES2-7)

Sample No.	Alloy	Sample Mass (g)	Inoc. (Wt Pct)	Cooling Condition (°C)
ES1-1	S0.061	3.8	0.3 S.Sd	Q-1170
ES1-4	S0.028	4.14	0.3 S.Sd	Q-1170
ES1-5	S0.007	3.93	0.3 S.Sd	Q-1280
ES1-6	S0.061	9.11	0.5 Al	Q-1250
ES1-7	S0.061	15.5	0.2 Ti	S.C
ES1-8	N-Mn	0.46	1.0 S.Sd	Q-1300
ES1-9	L-Mn	0.68	1.0 S.Sd	Q-1300

Q, quenching; Inoc., inoculation; S.Sd, Superseed[®] inoculant; S.C, slow cooling.

Table III. Samples Inoculated with Superseed[®] inoculant

Sample No.	Alloy	Sample Mass (g)	S. Sd Inoc. (Wt Pct)
ES2-10a	S0.107	5.25	0
ES2-10b	S0.061	4.9	0
ES2-10c	S0.028	5.04	0
ES2-10d	S0.021	4.03	0
ES2-10e	S0.010	4.05	0
ES2-10f	S0.007	3.03	0
ES3-11	S0.107	5.04	0.5
ES3-12	S0.061	4.58	0.5
ES3-13	S0.028	5.04	0.5
ES3-14	S0.021	4.58	0.5
ES3-15	S0.010	4.04	0.5
ES3-16	S0.007	3.02	0.5
ES4-24	N-Mn	7.98	0
ES4-25	N-Mn	7.06	0.5
ES4-26	L-Mn	6.6	0
ES4-26	L-Mn	6.66	0.5

The cooling rate was approximately 60 K (°C)/min for all samples.

Table IV. Uninoculated Samples Melted in a Differential Scanning Calorimeter (DSC) at a Cooling Rate of 15 K (°C)/min

Sample No.	Alloy	Sample Mass (mg)
DSC-17	S0.107	128
DSC-18	S0.061	157
DSC-19	S0.028	230
DSC-20	S0.021	147
DSC-21	S0.010	167
DSC-22	S0.007	210
DSC-23	N-Mn	170

analysis of the quenched samples, it was found that almost all of the graphite particles were nucleated by the (Mn,Mo)S with oxides, type of inclusions. The absence of Mn in the base alloy is interesting because graphite was nucleated by a small particle ($\leq 1 \mu\text{m}$) consisting of SrO and a complex compound of Ca with Mo as sulfide (ES1-9) (Figure 1(d)).

A higher concentration of aluminum (0.5 wt pct, ES1-6) caused the formation of aluminum nitride, which nucleated MnS (Figure 1(f)). In the lower sulfur content

(0.028 pct, 0.007 pct) samples (Figure 1(b,c)), the ratio between S and Mo was reduced compared to the data in Figure 1(a), despite the fact that Mn and S contents in the alloys were similar. AlN particles could not nucleate graphite. Similarly, Ti (0.2 wt pct, ES1-7) formed a complex particle containing TiN and Mo₂C (Figure 1(e)); however, these particles could not nucleate graphite.

By slowly cooling the sample (ES4-24), we discovered Mo forming a complex compound with Cr which could be interpreted as (Mo,Cr)S, that seems to have nucleated graphite and then grown together with graphite (Figure 1(g)). In the N-Mn alloy that was not inoculated, (Mo,Cr)S was often observed with round edges and a flake-like structure. A similar observation was made by inoculating sample ES4-25. A Mo₂C phase was found in addition to graphite and (Mo,Cr)S (Figure 1(h)). The Mo₂C phase was also observed in samples containing 0.6 wt pct of Mn, such as sample ES1-1; but in this sample, we did not find any (Mo,Cr)S particle.

B. Effect of Sulfur and Inoculation on MnS Growth Morphology

MnS grew in a variety of shapes. Some MnS inclusions had iron particles in the center or off to one side, which might have been the result of the cutting plane. In uninoculated samples with higher sulfur content, large size MnS inclusions of a variety of shapes were found, connected with graphite flakes (Figures 2(a) through (d)). A significant modification in the growth morphology of MnS was observed at lower MnS particle sizes (Figures 2(e) through (i)). In this case, MnS grew as a faceted cubic structure on complex oxides. Straight, thick, and long graphite flakes (compared to uninoculated samples) were nucleated on the MnS particle (Figures 2(e) through (i)). Other shapes of MnS, such as the hexagonal, triangular, or trapezoidal forms, occurred as a result of the different cutting planes associated with MnS particles, hereby referred to as regular MnS particles (while all other shapes would be categorized as irregular MnS particles). A statistical analysis was performed on the uninoculated samples ES2-10a to ES2-10f and inoculated samples ES3-11 to ES3-16 (Table III). The shapes and sizes of MnS particles were recorded from 6 adjacent SEM images at a randomly chosen location of the polished surface, covering a total area of analysis equal to 2.248 mm². A significant difference was observed in the shape of MnS particles, depending on whether the samples were inoculated or uninoculated. Above a certain limit of sulfur (e.g., 0.021wt pct), MnS particles were regular, but by increasing the sulfur content, MnS particles' growth becomes unstable and irregular-shaped particles were obtained. MnS nucleation on Oxides or sulfides (Al₂O₃, SiO₂, SrO, CaO, and CaS) brings stability in growth to MnS and modifies growth morphology from an irregular to a regular faceted cubic structure, even at a higher sulfur concentration (Figure 3). Due to more number of nucleation sites for MnS nucleation, the size of MnS will decrease accordingly as shown in Figure 3. In the absence of oxides in the melt, MnS grew with an irregular geometry consisting of small and large sizes

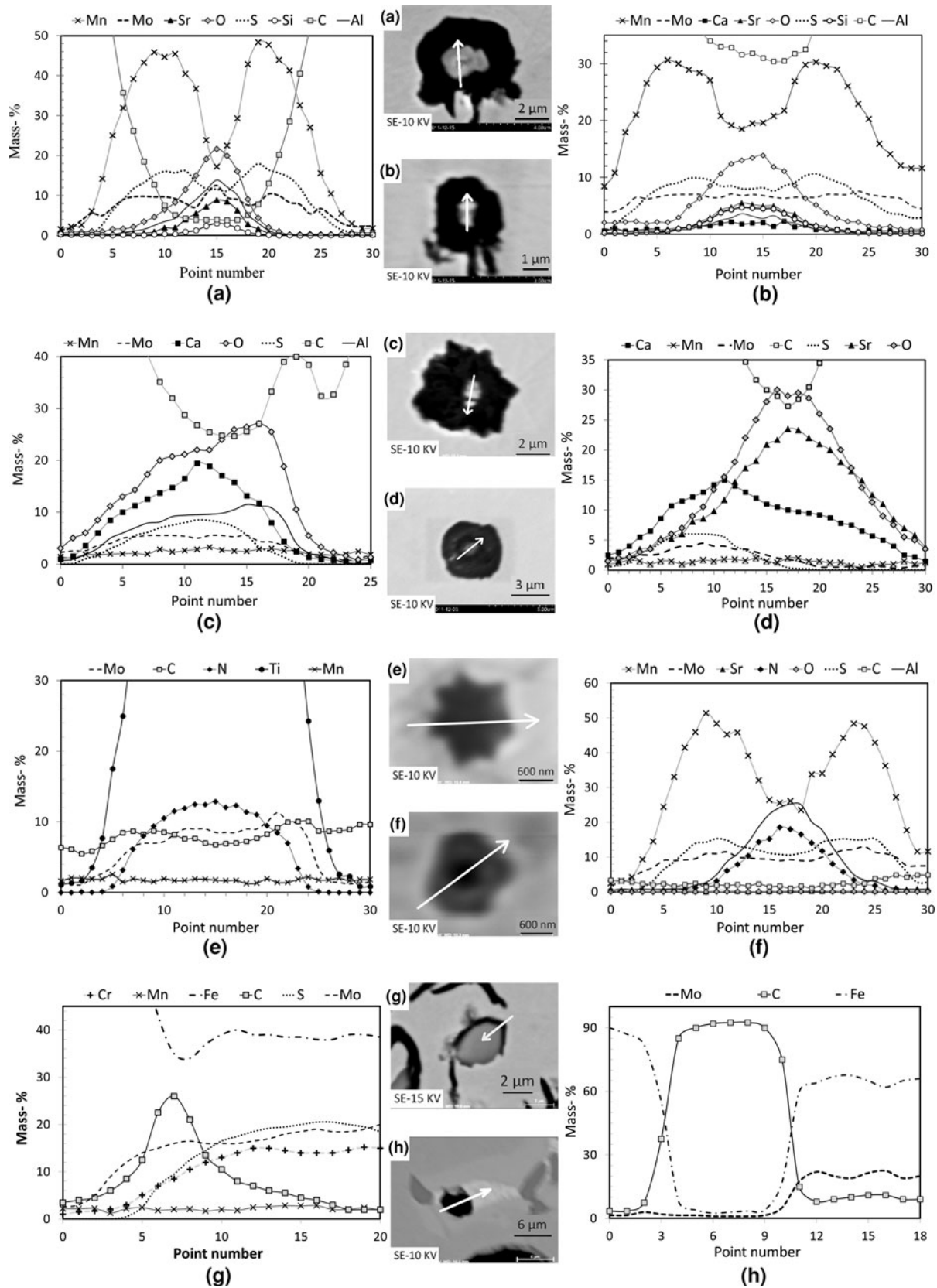


Fig. 1—EDX line analysis. (a) Sample ES1-1: Al_2O_3 , SiO_2 , SrO , $(\text{Mn},\text{Mo})\text{S}$, and graphite. (b) Sample ES1-4: Al_2O_3 , CaO , SiO_2 , SrO , $(\text{Mn},\text{Mo})\text{S}$, and graphite. (c) Sample ES1-5: complex compound of $(\text{Mo},\text{Ca})\text{S}$, Al_2O_3 , traces of Mn and graphite. (d) Sample ES1-9: SrO , $(\text{Mo},\text{Ca})\text{S}$ and graphite. (e) Sample ES1-7: TiN , Mo_2C without graphite. (f) Sample ES1-6: AlN , $(\text{Mn},\text{Mo})\text{S}$ without graphite. (g) Sample ES4-24: $(\text{Mo},\text{Cr})\text{S}$ compound, traces of Mn and graphite. (h) Sample ES4-24: Mo_2C and graphite.

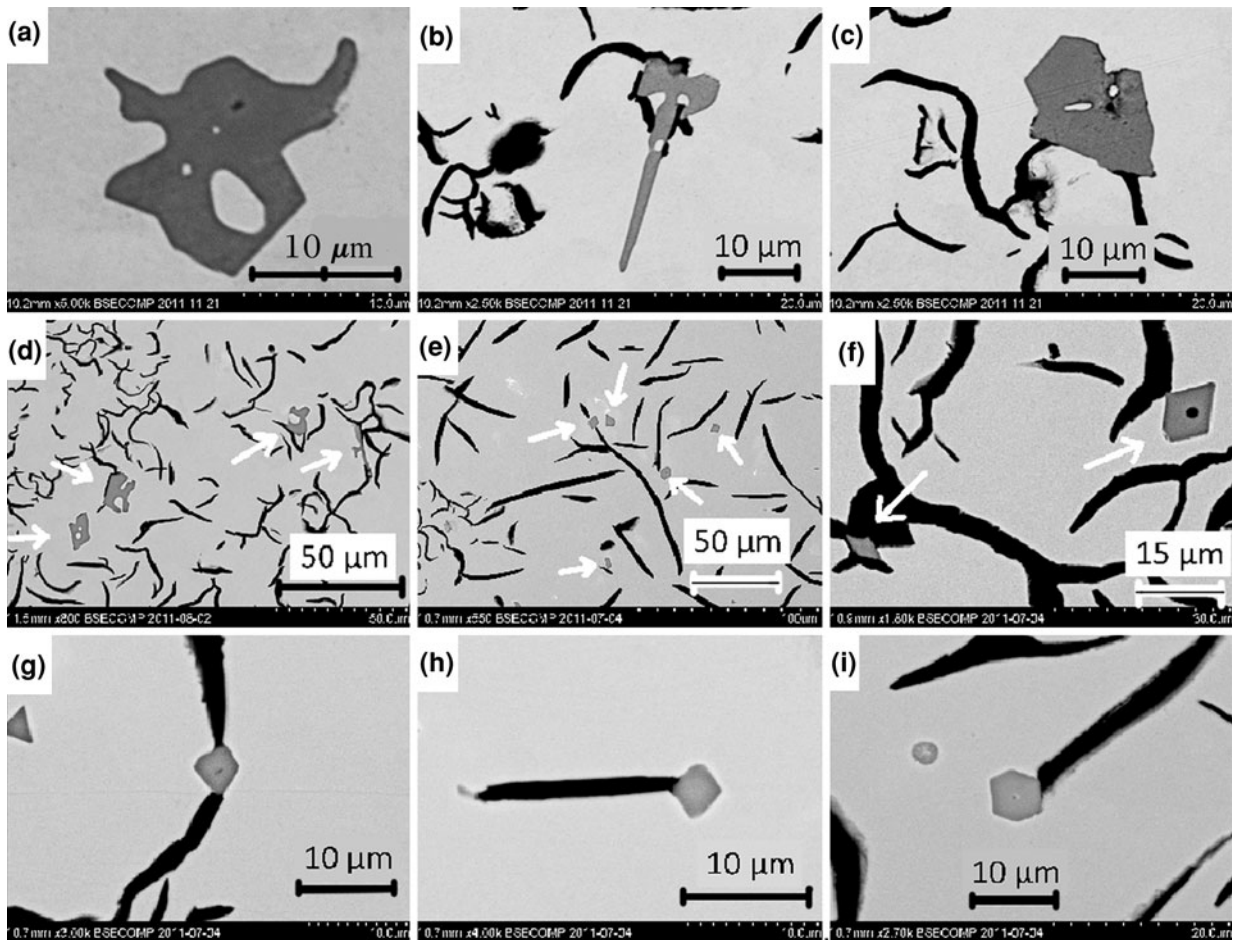


Fig. 2—Growth morphologies of MnS. (a, b, c, d) Uninoculated sample ES-10a. (e, f, g, h, i) Inoculated samples ES3-11 and ES3-12.

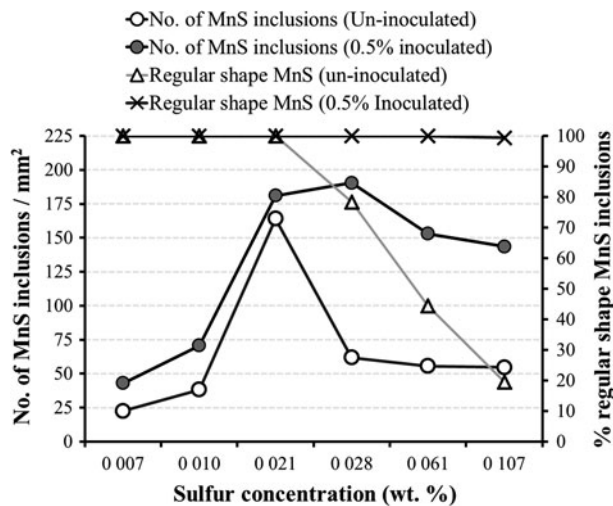


Fig. 3—Statistic analysis of size distribution and percent regular shapes of MnS in inoculated and uninoculated samples at different sulfur concentrations in the base alloys.

according to the amount of sulfur present in the alloys (Figures 2(a) through (c)). Below a sulfur content of 0.028 wt pct, all MnS particles were regular in shape (Figure 3).

The number of MnS particles increased considerably due to more number of nucleation sites for MnS nucleation, at the cost of reduction in their sizes, in the samples with sulfur contents greater than 0.021 pct (Figure 3). A majority of MnS inclusions were large in samples with a high sulfur content, but as the sulfur content decreased, smaller MnS inclusions became dominant (Table V). With a decreasing MnS particle size, the number of MnS inclusions increased up to a certain sulfur concentration. Inoculated samples demonstrated a significant reduction in the size of MnS inclusions. Particularly, the alloys containing high sulfur content, such as ES3-11 (S 0.107 pct) and ES3-12 (S 0.061), when inoculated, resulted in a 50 and 39 pct increase, respectively, in small size (0.5 to 2 μm) of MnS particles (Table V). In the last sample ES2-10f (S 0.007), only one size of MnS particles was observed (Table V).

C. Influence of Inoculation and Sulfur on Graphite Growth Morphology

This section addresses the results of the ES2, ES3, and DSC experiments (Tables III, V). The sulfur content in the alloy influences the graphite morphology to a large extent. When we observed the uninoculated samples, the graphite morphology appeared to change from type-A

Table V. MnS Particles Size Distribution for Different Sulfur Contents and Melt Treatment

[S] Wt Pct	Average Particle Size (μm)				
	≥ 12	8 to 12	5 to 8	3 to 5	0.5 to 2
	Percentage of MnS Inclusions				
0.107	18.7	42.3	24.40	13.8	0.81
0.061	8.0	30.4	47.20	14.4	0.00
0.028	0.0	0.0	31.60	59.0	9.35
0.021	0.0	0.0	0.81	16.3	82.90
0.007	0.0	0.0	0.00	0.0	100.00
Inoc.	0.0	1.9	13.60	33.1	51.40
0.107					
Inoc.	0.0	0.3	16.60	43.9	39.20
0.061					
Inoc.	0.0	0.0	2.80	40.6	56.50
0.028					

graphite structure to an interdendritic flake graphite (course type, oriented between the dendrites) and undercooled fine graphite (ultrafine flake graphite, interconnected with each other) structure between the dendrites, as shown in Figures 4(a) through (d). Inoculants resulted in randomly oriented type-A graphite structure (Figures 4(e) through (g)). In the samples with a sulfur content of less than 0.01 pct, the inoculants could not avoid the formation of an undercooled fine graphite structure (Figure 4(h)). After a deep etching of the sample with a sulfur content of 0.01 pct, the undercooled region of fine graphite had an interconnected network with fine graphite flakes (Figure 4(l)). Those samples having a high sulfur content (0.107 wt pct) were melted and cooled slowly to room temperature in the DSC resulted in interdendritic and oriented graphite structures (Figure 4(i)). In the sample $S = 0.028$ pct, the graphite structure was partly interdendritic with a small fraction of undercooled fine graphite structure. Samples with sulfur contents less than 0.028 exhibited completely undercooled fine graphite structures (Figures 4(k), (l)). After a careful analysis of the sample with $S = 0.021$ pct, a few small-sized ($\leq 1 \mu\text{m}$) MnS particles were observed at the periphery of austenite dendrites, but MnS particles could hardly be observed in the sample with $S = 0.01$ pct as the sulfur quantity was lower, while keeping in mind the non-equilibrium solidification which may not match the theoretic predictions (Figure 4(l)).

D. Graphite Growth Morphologies in the Absence of Mn in the Alloy

This section addresses the results of the ES4 experiment (Table III). The sample with a high sulfur concentration (ES4-24; N-Mn alloy) and without inoculation contained undercooled fine graphite and highly branched fine graphite flakes (Figure 5(a)). This form of graphite is called form II of flake graphite or Crab Form graphite. (Mo,Cr)S was precipitated along the graphite flakes, especially in highly branched areas. In Figure 5, Mo₂C appears bright and (Mo,Cr)S appears in gray contrast. The Mo₂C phase was observed primarily in

elongated and fine mesh shapes in areas that were either attached to graphite flakes or (Mo,Cr)S particles as seen by the bright areas in Figure 5(a).

In the uninoculated samples with lower sulfur concentration (ES4-26, Table III), the fraction of fine undercooled graphite was larger (Figure 5(c)). This is in agreement with the results shown in figure 4(c) of a sample containing Mn. The branching phenomena associated with graphite reduced and fewer (Mo,Cr)S particles were observed in the microstructure (as expected due to lower sulfur content). Inoculation played a dominant role in modifying the structure of graphite in both alloys and in diminishing the fine undercooled regions through the growth of graphite in an interdendritic manner; however, the growth of graphite flakes was to some extent random in the sample containing high sulfur content (N-Mn). Nevertheless, many (Mo,Cr)S particles still existed in the structure in connection with graphite and Mo₂C. The N-Mn alloy ($S = 0.09$ pct) was melted and solidified in the DSC equipment at a cooling rate of 15 K (°C)/min and without inoculation, which resulted in mostly an interdendritic flake graphite structure together with phases of (Mo,Cr)S and Mo₂C (Figure 6).

IV. DISCUSSION

Inoculants are added to the melt at a high superheat and they dissolve quickly after the addition. Wang *et al.*^[19] have shown that ferro-silicon particles will reach the temperature of the melt within a fraction of a second. Experiments showed that the formation of oxides/sulfides at a certain temperature in the melt or during the solidification depends on the concentration of the deoxidizers (Al, Sr, Ca, *etc.*) and sulfide-forming elements (Ca, Mo, Mn, *etc.*). The nucleation of any oxide/sulfide particle at different superheats or during the solidification process could change the growth morphology of the complex oxide-sulfide particle that can affect the nucleation of graphite in different ways. The sequence of nucleation of oxides/sulfides is important to understand because this helps in finding out the

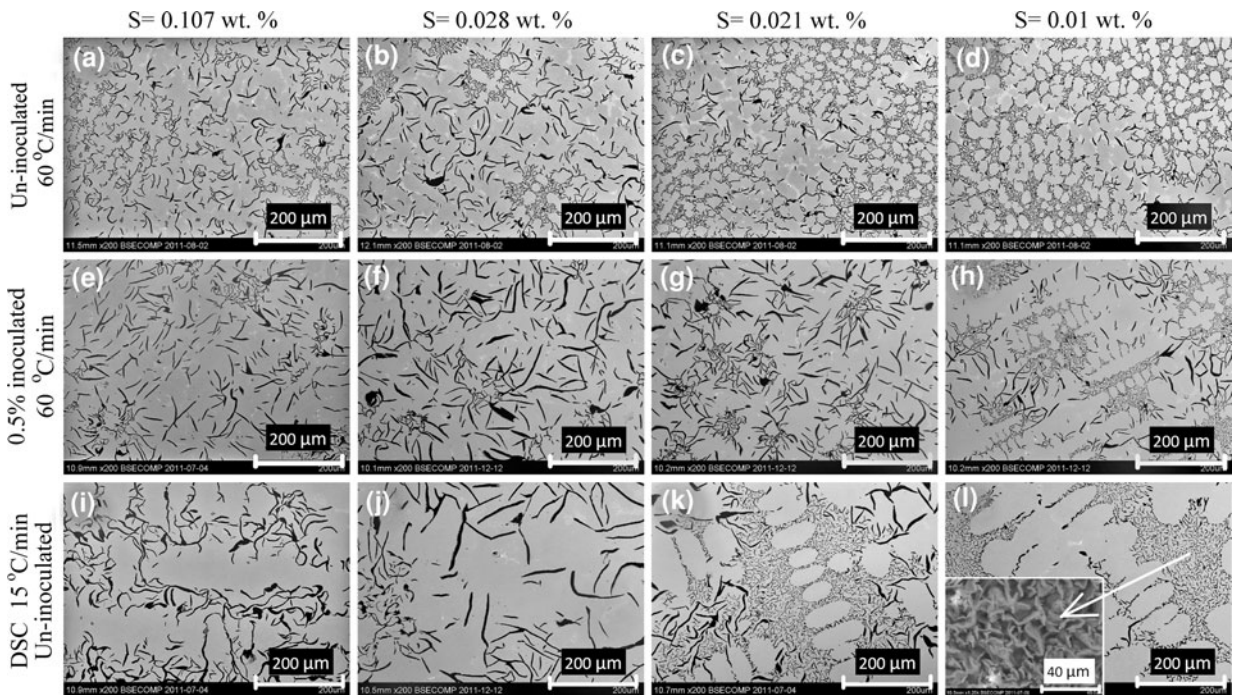


Fig. 4—SEM (BSE) images of different graphite growth morphologies at four different sulfur concentrations ($S = 0.107, 0.061, 0.028, 0.01$ wt pct) and treatments. (a, b, c, d and i, j, k, l) Uninoculated, (e, f, g, h) 0.5 wt pct inoculated. Each column of images shows the same sulfur concentration in the samples.

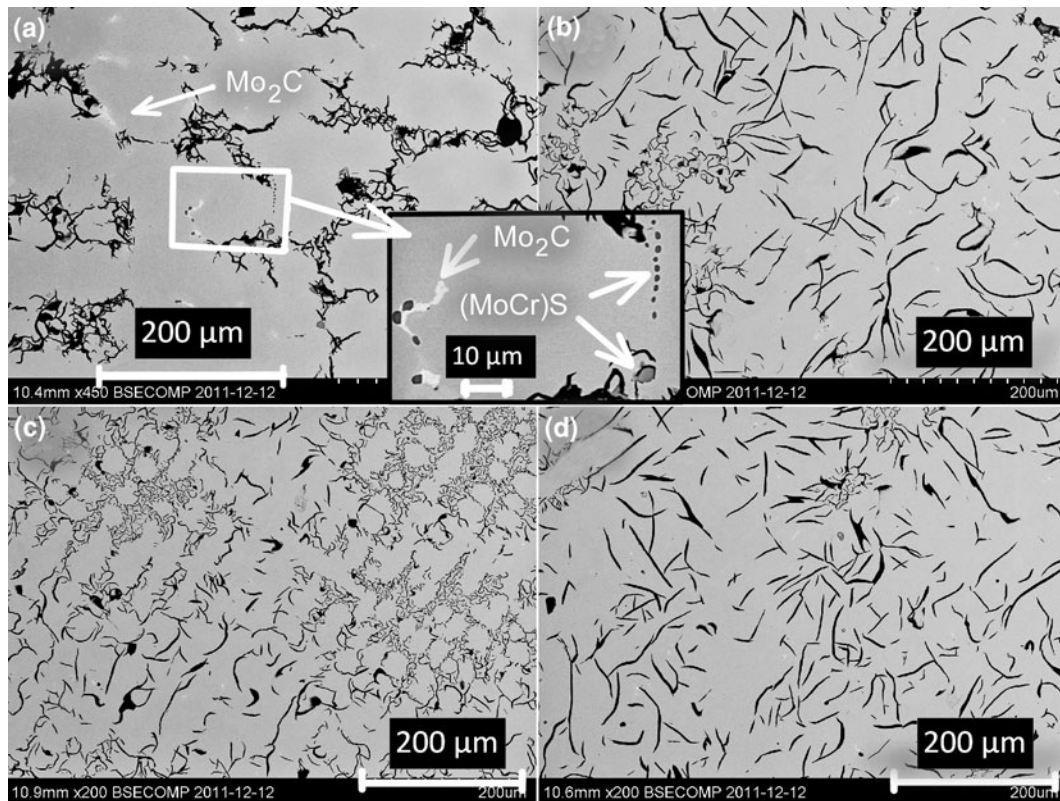


Fig. 5—Graphite growth morphologies in the absence of Mn in the alloy. Slow cooling of the alloys N-Mn and L-Mn. (a) N-Mn alloys, uninoculated. (b) N-Mn alloy, 0.5 wt pct inoculated (c) L-Mn alloy, uninoculated, and (d) L-Mn alloy, 0.5 wt pct inoculated.

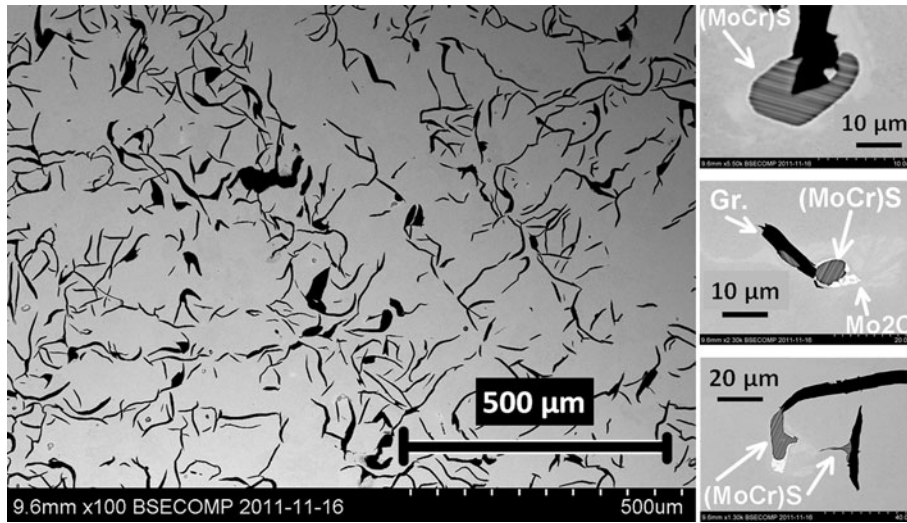


Fig. 6—(Mo,Cr)S in connection with graphite together with Mo₂C. Uninoculated N-Mn alloy melted and solidified in the DSC at a rate of 15 K (°C)/min. Small images show (Mo,Cr)S and Mo₂C (appears bright) together with graphite.

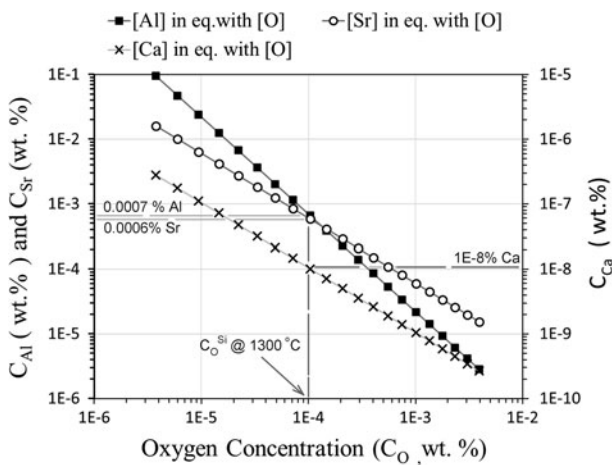


Fig. 7—Thermodynamic equilibrium between oxygen and Al, Sr and Ca in the cast iron melt at a temperature of 1573 K (1300 °C). ($C_{Si} = 1.93$ wt pct).

appropriate concentration limit of an inoculant. The nucleation of oxide/sulfide particle during solidification can happen when the concentration of an inoculant and oxygen/sulfur is enough in the melt to achieve the supersaturation limit of homogeneous nucleation of the oxide/sulfide particle. The possibilities of forming different kinds of oxides/sulfides and their sequence of nucleation in the melt and during the solidification process will be analyzed using thermodynamics, with a comparison to the experimental results.

A. Thermodynamic Study of Inoculants

1. Formation of oxides

Basic thermodynamic models are applied to investigate the possibility of nucleating Al₂O₃, SrO, SiO₂, and CaO. Detailed calculations are provided in the Appendix. Oxygen concentration in the liquid cast iron is

available in two forms: oxygen dissolved in the melt and oxygen present in a combined state as FeO or SiO₂. Each element of an inoculant has different affinity toward oxygen, which causes the nucleation of those oxides at a certain oxygen concentration in the melt. The solubility of oxygen decreases in the melt with decreasing temperature. The equilibrium amount of Al, Sr, and Ca with oxygen was calculated (see Appendix for each element) using the simple thermodynamic function in Eq. [1].

$$\frac{a_M^m \cdot a_O^n}{a_{M_m} a_{O_n}} = \exp\left(\frac{-\Delta G^\circ}{RT}\right) \quad [1]$$

where a_M and a_o are the activities of the metal atoms and oxygen atoms in the melt, respectively. $-\Delta G^\circ$ is the standard free energy of the reaction, R is ideal gas constant, and T is temperature in kelvin units.

It is assumed that the dissolved oxygen in the melt remains in equilibrium with the dissolved Si in the iron, which also implies equilibrium between Si and SiO₂. The dissolved oxygen concentration in the melt in equilibrium with Si (C_O^{Si}) was calculated at a temperature of 1573 K (1300 °C), which is 0.0001 wt pct at the given Si concentration (1.93 wt pct). At a 0.0001 wt pct oxygen concentration, the equilibrium amounts of Ca, Al, and Sr are approximately 1e-8, 6.55e-4, and 5.84e-4 wt pct, respectively (Figure 7). At these values of C_{Al} and C_{Sr} initially in the melt, the nucleation of Al₂O₃ and SrO may not be possible at a temperature close to 1573 K (1300 °C) or above, but at lower temperatures close to the freezing point of the melt, the given amount of Al and Sr (0.0007 pct Al and 0.0006 pct Sr) will be more than the required limit to get in equilibrium with oxygen which can cause nucleation of the oxide particles. Typically, the amount of added Ca are higher than the required amounts for equilibrium with oxygen over the given range of oxygen concentration as shown in Figure 7; hence, it is possible to homogeneously nucleate CaO at an early stage of inoculation.

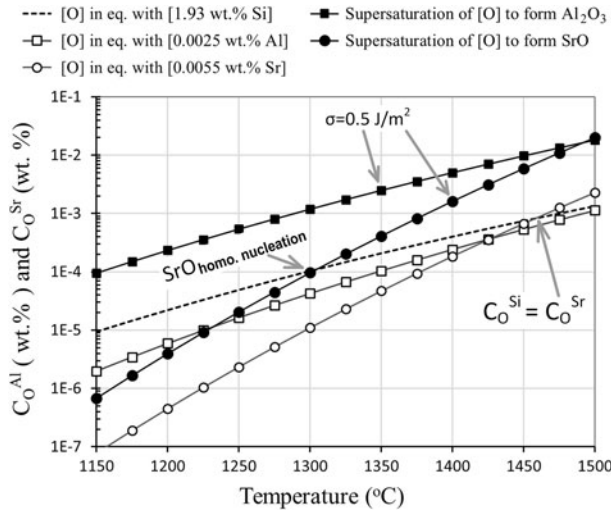
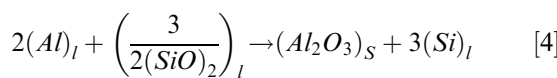
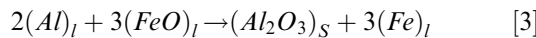
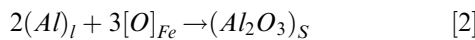


Fig. 8—Concentration of oxygen in the equilibrium with added Al (C_O^{Al}) and Sr (C_O^{Sr}) corresponding to 0.5 wt pct of Superseed[®] inoculants. C_O^{Si} represents the available dissolved oxygen content.

2. Utilization of dissolved oxygen

The oxygen concentration in the melt has a significant influence on the nucleation of oxides and consequently modifying the graphite structure. Ekengård *et al.*^[20] reported the importance of oxygen in the melt, whereby high oxygen content favors the growth of graphite flakes. Lietaert^[21] reported that during the solidification process, the interfacial energy is reduced by the absorption of oxygen and sulfur at the boundary of the graphite and the melt, which affects the growth of graphite during the cooling process. Ten^[22] found experimentally that a high saturation of cast iron melt with oxygen increases the tendency of the modification of graphite to a favorable structure. A high oxygen concentration can be undesirable when pure Ca is used as inoculant that causes the formation of CaO instead of CaC₂, as reported by Fraš *et al.*^[23] They have shown that CaC₂ increases eutectic cell count, but the formation of CaO reduced the cell count.

It is obvious that high oxygen content will increase the number of oxides nuclei which will provide nucleation sites for MnS. Oxides are formed either by a direct reaction between the dissolved oxygen in the melt and the metal atoms (*e.g.*, Al, Sr, and Ca) or by a deoxidation reaction with either SiO₂ or FeO, which is available in the melt as an undissolved form of oxygen according to De Sy.^[24] (Subscript “Fe” shows element dissolved in the base iron melt; “s” solid state; “l” liquid state.)



A similar reaction is expected for the other oxide stabilizing elements as well. Some quantity of metal,

such as Al or Sr, might remain unreacted with oxygen or another compound due to the low concentration of oxygen and the necessary amount of Al or Sr needed to achieve the required limit for nucleation of Al₂O₃ or SrO. The supersaturation of metal atoms (M) and dissolved oxygen or sulfur (N) for nucleation was calculated using Eq. [5]. (See notations Appendix.)

$$C_M^X \cdot C_N^Y = (C_M^X \cdot C_N^Y)_{eq} \exp \left[\frac{\sqrt{\frac{16\pi\sigma^3 (V_m^{M_x N_y})^2}{3 \cdot K_B 60 T}}}{RT} \right] \quad [5]$$

For the homogeneous nucleation of oxide/sulfide, a certain amount of combined supersaturation of the metal atoms and oxygen/sulfur is required to grow stable nuclei in the melt. The steeper the equilibrium line (between the metal and oxygen/sulfur, plotted vs temperature), the faster the supersaturation limit is reached. In Figure 8, the equilibrium line of C_O^{Sr} is steeper than that of C_O^{Al} ; hence, one type of particle will nucleate sooner than the other (for the concentrations given in Figure 8), resulting in the reduction of dissolved oxygen concentration. A supersaturation limit must be achieved by metal atoms to form oxide or sulfide particles. The available oxygen concentration which is in equilibrium with Si (Figure 8) is decreasing with temperature drop, but it (C_O^{Si}) should appear above the other lines to create situations where the required limit for supersaturation of oxygen (to form oxide) is less than the available oxygen concentration (C_O^{Si}). If the oxygen concentration is below the required amount for nucleation for any oxide, then no more oxides will be formed in the melt prior to solidification. According to Eq. [5], the supersaturation level depends on the surface tension (σ) between the inclusion oxide and the surrounding melt. For a SrO particle, this value is not accurately estimated; however, we used a value of $\sigma = 0.5 \text{ J/m}^2$ as an example (Figure 8). At this value oxygen is in a supersaturated state for the homogeneous nucleation of SrO at 1573 K (1300 °C) temperature. But, the supersaturated limit of oxygen for Al₂O₃ formation could not be achieved at a value of $\sigma = 0.5 \text{ J/m}^2$.

3. Thermodynamic study of sulfides

Sulfur is dissolved in the melt in atomic form. Based on EDX analysis of the particles formed during the inoculation process, a variety of sulfides were found that are formed either together with the oxides/sulfides or alone, such as CaS, (Mn,Mo)S, (Ca,Mo)S, and (Mo,Cr)S. A certain amount of Mo was always found in the MnS particles together with the oxides/sulfides, such as SrO, Al₂O₃, SiO₂, and CaS. Different types of sulfides have particular growth morphologies at a fixed sulfur concentration in the melt. Using thermodynamic analysis, the possibility of nucleating these sulfides prior to solidification was investigated.

In Figure 9, thermodynamic equilibrium values of sulfur with a given concentration of Mn are provided (avg. $C_{Mn} = 0.60 \text{ wt pct}$) at 1473 K, 1573 K, and 1673 K (1200 °C, 1300 °C, and 1400 °C) temperature

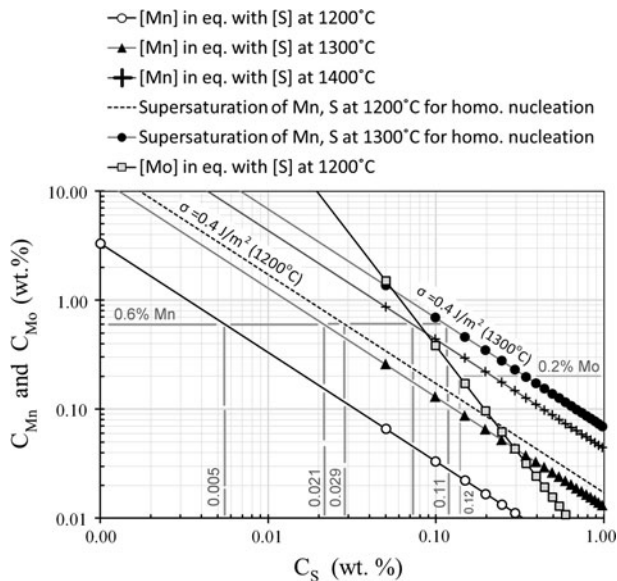


Fig. 9—Thermodynamic equilibrium between Mn, Mo, and S, and the required supersaturation to form MnS homogeneously in the melt at 1473 K and 1573 K (1200 °C and 1300 °C).

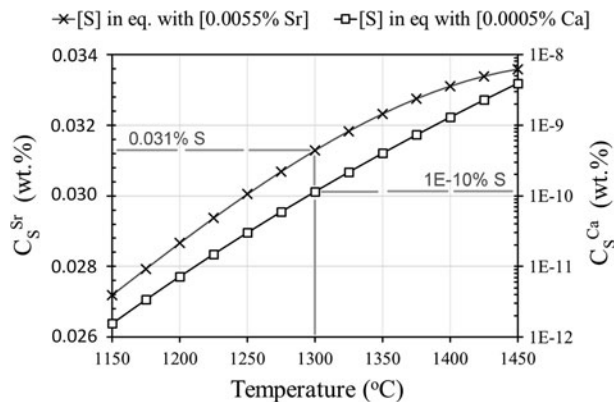


Fig. 10—Concentration of S in equilibrium with 0.0055 wt pct Sr and 0.0005 wt pct Ca corresponds to 0.5 wt pct Superseed[®] inoculants at different temperatures.

are 0.005, 0.021, and 0.071 wt pct, respectively. According to microstructure examination of sample DSC-20 ($S=0.021$ pct, Table IV), few small MnS particles ($<1 \mu\text{m}$) were observed on the austenite periphery. Additionally, a (virtually) complete undercooled fine graphite structure was obtained as a result of lower sulfur content and MnS could not be nucleated (Figure 4(l)). Similarly, sample DSC-19, with slightly higher sulfur content ($S0.028$), resulted in plenty of small MnS particles in the austenite (Figure 4(j)), while undercooled fine graphite flakes were absent. One should remember that fine undercooled graphite are not nucleated by MnS. From these observations (Figures 4(k), (j)), the value of supersaturation for MnS can be estimated as $(C_{\text{Mn}}C_{\text{S}})_{\text{initial}}/(C_{\text{Mn}}C_{\text{S}})_{\text{eq}} = 5.21$ ($C_{\text{Mn}} = 0.6$, $C_{\text{S}}^{\text{initial}} = 0.025$ (assumed), $C_{\text{S}}^{\text{eq}} = 0.0048$). The product values above are based on the equilibrium conditions, but experimentally it is difficult to achieve the equilibrium

conditions for solidification. Nevertheless, for practical applications, the given product reaction values are useful.

It was also noteworthy that Mn and Mo sulfides nucleated together in samples containing Mn and Mo as the alloying elements (Figure 1). This can most likely be explained by the simultaneous growth of MnS with MoS_2 , as shown in Figures 1(a, b). In all of our alloys, the concentration of Mo was between 0.15 and 0.22 wt pct. By considering the formation of molybdenum sulfide as MoS_2 , according to the equilibrium analysis between Mo and S at 1473 K (1200 °C), the required sulfur concentration is 0.12 wt pct in equilibrium with 0.2 wt pct Mo (Figure 9). Obviously, a MoS_2 particle could not have been nucleated in the melt prior to solidification due to the low sulfur content in the alloys (provided that there was no element (*e.g.*, Sr, Si, or Al) in the melt that could increase the activity of Mo toward sulfur). In all quenching experiments, Mo was observed incorporated with other sulfides and oxides while surrounded by graphite (Figure 1(d)). It might be possible to form MoS_2 through microsegregation due to very low partition coefficient value of Mo. In the absence of Mn, complex sulfide $(\text{Mo,Cr})\text{S}$ was observed, which is a non-faceted structure and grows in many different shapes, such as flakes or other geometries that are round and irregular. It was often found attached to graphite. It seems that $(\text{Mo,Cr})\text{S}$ has nucleated graphite and that the complex continued to grow together with graphite as a particle (or as a flake) along the graphite flake. A highly branched graphite structure was obtained together with $(\text{Mo,Cr})\text{S}$ precipitation. $(\text{Mo,Cr})\text{S}$ precipitates along the graphite flake lengthwise and covers some area of the flake, further growth of the graphite flake on that particular side would likely cease, which could create conditions for the graphite to grow in branches away from the main graphite flake, thus generating the crab form of graphite.

The possibility of SrS formation in the melt was studied using thermodynamics. The sulfur content in equilibrium with Sr at different temperatures is shown in Figure 10. Sulfur in equilibrium with 0.0055 wt pct Sr (0.5 wt pct of Superseed[®] inoculants) in the liquid was in the range of 0.026 to 0.034 wt pct (Figure 10). If we assume a SrS particle surface tension of $\sigma = 0.5 \text{ J/m}^2$, the required supersaturation level of Sr for the homogeneous nucleation of SrS at 1673 K (1400 °C) is 0.011 pct at a sulfur concentration of 0.1 pct (which is two times greater than the added amount of Sr (0.0055 wt pct)). In this case, the homogeneous nucleation of SrS prior to solidification is not possible. The interaction coefficient between Sr and other elements in our alloy might change the calculation result. Similarly, the interaction coefficient between Ca and S is not known, and this could also affect the equilibrium calculations. The equilibrium concentrations of S and Ca at different temperatures vary from $1\text{e-}8$ to $1\text{e-}12$ wt pct, which are quite low compared to typical sulfur content in cast iron (Figure 10). Therefore, sulfur is already sufficiently supersaturated to homogeneously nucleate CaS at the casting temperature of the alloy.

Assuming that all of the Ca will be consumed to form CaS particles, we can calculate the remaining sulfur

content in the sample by mass balance. The consumption of sulfur due to CaS and SrS formation is very small and can be neglected. Thus, we can assume that all of the sulfur in the alloy is available for Mn and Mo to form sulfides according to our alloy composition. For oxides, the problem is more complicated due to the stepwise consumption of dissolved oxygen during oxide formation, and it is difficult to estimate the remaining oxygen concentration in the melt after the oxides formed.

4. Sequential nucleation of oxides/sulfides and its effect on graphite growth morphology

From thermodynamic study of oxides and sulfides as well as from the experimental results regarding graphite growth morphologies, it was found that the nucleation of a certain phase (oxides and sulfides) at a certain temperature affects the growth morphologies of MnS and graphite. In the samples with high sulfur contents (ES2-10a and ES3-11b), MnS particles were quite large in size. As can be seen in Figure 9, at a sulfur concentration of 0.11 pct S, MnS will nucleate homogeneously at 1573 K (1300 °C) and continue to grow in the melt during cooling. This will result in larger size but less number of MnS inclusions (without considering its nucleation on oxides). By decreasing the sulfur concentration in the alloy to 0.061, 0.028, and 0.021 wt pct while keeping Mn concentration constant (0.6 wt pct), nucleation of MnS will shift to lower temperatures and the size of MnS particles will remain smaller due to insufficient time for growth.

Since oxides provide nucleation sites for MnS, it is important to first nucleate oxides in the melt to provide a substrate on which MnS can grow. The precipitation of MnS should be suppressed by reducing the S or Mn concentration to a level at which Mn and S would be supersaturated just before solidification. As a result, a large number of small MnS particles will heterogeneously nucleate on the existing oxides and a large number of fine graphite flakes will be nucleated on MnS particles prior to solidification. Riposan *et al.*^[12] mentioned a similar concept involving a three-stage model for the nucleation of graphite that starts with oxides and then proceeds to MnS and finally graphite.

At higher solubility values of Mn and S, oxide formation and MnS nucleation occur at the same time. This results in the simultaneous growth of MnS and oxides, which leads to an irregular substrate on which graphite flake can nucleate. Thus, the graphite growth morphology will be modified in an undesirable manner.

Extensive work was performed by Goodrich *et al.*^[17] in investigating the influence of the Mn-to-sulfur ratio and relating it to the strength of the material. He showed that the ultimate tensile strength was highest at $C_{Mn}C_s = 0.0167$ and 0.0126 wt pct². For the solubility product values of S and Mn, such as 0.0345, 0.0309, and 0.0544 wt pct², the ultimate tensile strength was less. By comparing these results to our thermodynamic calculations and experimental observations (Figures 4(h), (k)), at $C_{Mn}C_s = 0.6 \cdot 0.029 = 0.0178$ wt pct², MnS will nucleate homogeneously at a temperature close to 1473 K (1200 °C) just before solidification (considering

the supersaturation of Mn and S). As mentioned earlier, the nucleation of MnS just prior to solidification will produce preferred graphite morphology thus increasing the strength of the material. At higher solubility product values, MnS will nucleate at high temperatures and during cooling, it will grow to large size and adopt different growth morphologies that will influence the graphite growth structure and finally the strength of the material. This explains the results obtained by G. M Goodrich. Similarly, Muzmudar *et al.*^[1,2] obtained a minimum chill, maximum cell count and maximum tensile strength with reduced hardness at $C_{Mn}C_s = 0.01425$, 0.026 in the inoculated samples. These values of $C_{Mn}C_s$ are close to our result ($C_{Mn}C_s = 0.0178$ wt pct²) and demonstrate the influence of the solubility product on the mechanical properties of the material. Many authors, such as Sommerfeld *et al.*,^[16] Goodrich *et al.*,^[18] and Fraš *et al.*^[18] have stated the importance of Mn/S ratio; however, the factor controlling the nucleation of MnS and graphite is the solubility product of Mn and S for the same amount of Mn. Experiments showed that above a certain limit of S or Mn concentration in the alloy, an undesirable graphite structure is formed; hence, one should consider the solubility product values under those beneficial limits. For instant, Roula *et al.*^[25] reported that a Mn content in the alloy exceeding 1 pct starts to slow down graphite growth and promotes carbides instead due to kinetics. Similarly, a higher sulfur content such as above 0.1 wt pct produce a coarse type thick graphite flakes.

B. Modification of MnS Growth Morphology by Inoculation

MnS has a cubic crystal structure, but we might observe a few other shapes in the microstructure which are produced during polishing of the sample (Figure 2). In the absence of inoculants, MnS growth morphology

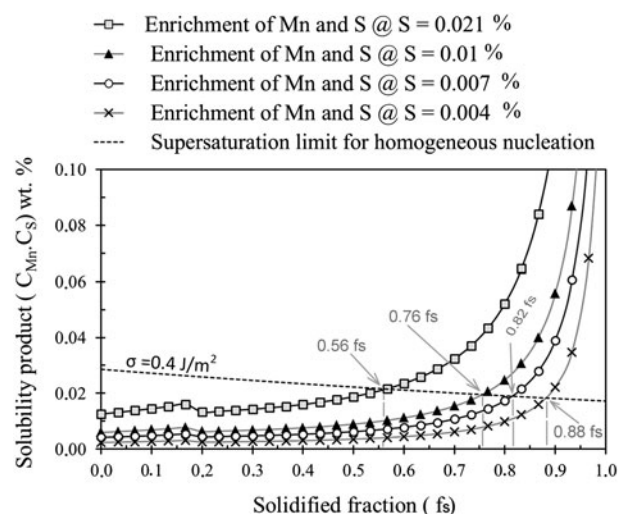


Fig. 11—Microsegregation of Mn and S in the melt vs fraction solidified and homogeneous nucleation of MnS at the given supersaturation limits.

adopts many different irregular shapes (Figure 2). The size of MnS particles increases with increasing sulfur content in the sample together with increasing irregularity.

In the experiments conducted in this study, we saw a remarkable modification of MnS particle growth morphology from an irregular to a regular structure due to the presence of oxide substrate for MnS nucleation (statistical results are shown in Figure 3). Through inoculation, the number of nucleation sites for MnS increases, resulting in a reduction of the size of MnS particles (Table V).

C. Supersaturation Mechanism and the Nucleation of New Oxide/Sulfide Particles During Solidification

During solidification, the remaining melt between dendrite arms becomes enriched in sulfur, oxygen, alloying elements, and some of the inoculants that are not fully consumed in the melt. Under these circumstances, the concentration of certain elements reaches the required supersaturation for the homogeneous nucleation of oxides or sulfide, and new nuclei will appear (as discussed previously by Magnusson^[26] in her Ph.D. thesis regarding nodular cast iron). The formation of new MnS particles can be predicted in terms of a solid fraction by mean of Scheil's Model of Segregation and Lever Rule. Detailed calculations are provided in the Appendix. The aim of this analysis was to determine the solid fraction at which new oxides and MnS particles can be nucleated in the remaining melt between the dendrites.

In this study, we observed that at 0.6 wt pct Mn and 0.028 wt pct S ($C_{Mn}C_S = 0.0168$ wt pct²), MnS was nucleated just before solidification (Figure 4(j)). In the thermodynamic equilibrium diagram (Figure 9), it is shown that MnS can be nucleated at 1473 K (1200 °C) (which is just above the freezing point of the alloy) homogeneously at a sulfur content of 0.029 wt pct (Mn = 0.6 wt pct) in the sample. Below this amount (0.029 wt pct S), such as 0.021 wt pct S, which is under the limit of supersaturation, MnS cannot be nucleated in the melt homogeneously. Therefore, it is assumed that the concentration of the remaining sulfur in the liquid at the freezing point of the melt was 0.021 wt pct, while the Mn content remained unchanged (0.6 wt pct) as no MnS inclusions had formed prior to solidification. The homogeneous nucleation of MnS depends on the equilibrium value of Mn with S as well as on the temperature and surface tension of the nucleated particles to remain stable in the melt and grow. The required supersaturation for the homogeneous nucleation of MnS and other particles in the interdendritic region was calculated considering a decreasing temperature condition as shown in Figure 11 [assumed solidification interval: 1473 to 1439.5 K (1200 to 1166.5 °C)]. It is assumed that no graphite is precipitated during the primary austenite formation and that the thermodynamic activities of all species (such as $a_{Sr,Al,S,O}$ etc) are unchanged due to changes in concentrations of the alloying elements (C, Si) and dissolved gases during the solidification. There is an accident in the enrichment curve. This is because of

not considering the effect of partition co-efficient of metal atom or gas phase (S, O) atoms on the graphite and austenite as well as the fraction of graphite formed according to our assumptions. The sudden drop appears during calculations when considering the effect of all the above-mentioned factors.

From our experimental results and thermodynamic analysis, MnS will nucleate when $(C_{Mn}C_S)_{initial}/(C_{Mn}C_S)_{eq} = 5.307$. The microsegregation of Mn and S in the melt during solidification depends on the initial concentrations of Mn and S in the melt at the freezing point of the melt. In Figure 4(k), very small MnS particles were observed at the periphery of the austenite dendrite, so it can be assumed that MnS will precipitate prior to solidification if $C_{Mn}C_S > 0.0126$, ($C_{Mn} = 0.6$, $C_S = 0.021$); if $C_{Mn}C_S < 0.0126$, it will nucleate during solidification due to microsegregation. In the former case, Mn and S will be consumed due to MnS formation in the melt. However, when the solubility product decreases to a value of 0.0126, it is difficult to precipitate MnS in the melt prior to solidification in the absence of inoculants. For alloys with $C_{Mn}C_S \geq 0.0126$, the supersaturation level of MnS will be achieved when 56 pct of the melt is solidified (Figure 11). This results in the formation of new MnS particles from homogeneous nucleation as predicted by the thermodynamic analysis. Moreover, for alloys with $C_{Mn}C_S \leq 0.0126$, MnS will nucleate at a solid fraction of >0.56 . According to this analogy, oxides would have to nucleate before 56 pct of the melt is solidified to provide nucleation sites for MnS (Figure 11).

In the samples of sulfur content less than 0.021 wt pct, mostly undercooled graphite was formed which can be compared to the thermodynamic results in Figure 11, which shows the homogeneous nucleation of MnS at solid fractions getting closer to 1. In practice, one cannot have equilibrium conditions of cooling; therefore, the homogeneous nucleation limit might not reach during solidification and the nucleation of MnS may not be possible.

In the case of Al_2O_3 and SrO nucleation between the dendritic arms, it is assumed that the concentrations of Al and Sr are the same as their initial concentrations, corresponding to the amount of inoculants added (Figures 12, 13). The oxygen content in the melt is assumed to be at equilibrium with Si as the temperature decreases during solidification. In practice, certain amounts of Al and Sr will be consumed to form their respective oxides prior to solidification, while the remaining amount will be utilized during the solidification process to nucleate new oxide particles. Al_2O_3 will nucleate homogeneously when $(C_{Al}^2C_O^3)_{initial}/(C_{Al}^2C_O^3)_{eq} \cong 1000$, ($\sigma = 0.75$ J/m²), and for the homogeneous nucleation of SrO, we can assume $(C_{Sr}C_O)_{initial}/(C_{Sr}C_O)_{eq} = 400$ and $\sigma = 1$ J/m². One approach to inoculation is to specify the composition of at least one inoculant (Al or Sr) to a concentration such that it can be nucleated as an oxide in the melt just after the primary austenite is formed. This situation would help to provide nucleation sites for the nucleation of MnS in the interdendritic region. During the eutectic reaction, these particles of MnS nucleated on oxides can provide

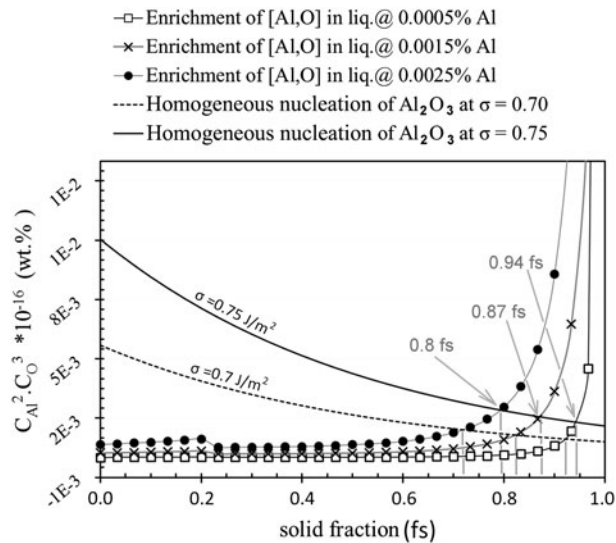


Fig. 12—Microsegregation of Al and O in the melt vs fraction solidified at different initial concentrations of Al, to nucleate Al_2O_3 homogeneously at different saturation limits.

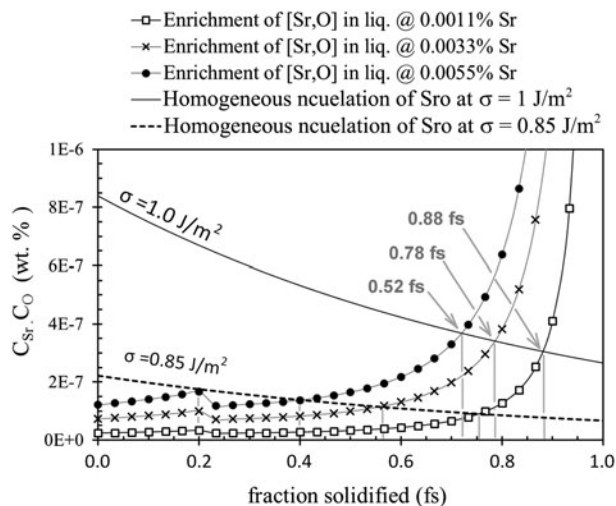


Fig. 13—Microsegregation of Sr and O in the melt vs fraction solidified at different initial concentrations of Sr, at given saturation limits.

nucleation sites for the graphite. Multiple supersaturation of the element in the melt during solidification are possible in some cases. In Figure 13, it is shown that SrO might nucleate at a solid fraction of 0.2, but the concentration will fall back to an equilibrium value. Again, Sr and O will become enriched, and new inclusions of SrO can be nucleated at another solid fraction. The nucleation of aluminum oxides can happen in the last stages of inoculation (Figure 12). The supersaturation of $C_{\text{Al}}^2 C_{\text{O}}^3$ has a strong dependence on the surface tension of the particle being nucleated. It is obvious from Figure 12 that Al_2O_3 can be nucleated only once due to its high saturation limit.

We observed numerous small MnS particles in the microstructure of all samples as shown in Figure 3 and Table V. From the size difference between the MnS

particles, it can be hypothesized that new MnS particles nucleated during solidification range in size from 0.5 to 2 μm . For example, if we examine the size distribution (average size) of MnS particles in sample ES3-13 (S0.028) without inoculation, the percentage of newly nucleated MnS particles (0.5 to 2 μm) is 9.35 pct (Table V). By inoculating the sample (ES3-13), the percentage of nucleated MnS particles during solidification increased remarkably to approximately 56.5 pct, while the percentage of larger MnS particles (3 to 5 μm) decreased by approximately 20 pct, as expected. Among the alloys with a sulfur content ≤ 0.021 wt pct, all of the MnS particles were nucleated during solidification (Table V). By inoculating these samples, no such enhancement was observed in the size distribution, but the number of MnS particles became almost twice the number of particles in the uninoculated samples with the exception of the 0.021 wt pct S content sample, as shown in Figure 3.

A similar trend was observed in the other samples of different sulfur contents as well. The common factor was that the nucleation of new oxides during the solidification increased the number of MnS particles at the expense of decreasing the number of large MnS particles that were formed prior to solidification. This situation will play an important role in providing new nucleation sites for graphite precipitation.

V. CONCLUSIONS

Inoculants produce oxides in the melt, which provides nucleation sites for MnS. With the increased number of nucleation sites, the number of MnS particles increases at the expense of a reduction in particle size. MnS particle adopts stable growth morphology when nucleated upon oxide. This has consequently improved the growth morphology of graphite. The graphite growth morphology depends on the type and the nucleation stage of the host nuclei in the melt. Using thermodynamics, one can predict the nucleation stage of any type of oxide or sulfide in the liquid or during the solidification. One can estimate the concentration of Mn and sulfur in a way that they are in a supersaturated state just before solidification starts, which will result in a large number of MnS-oxide particles that are nucleation sites for graphite flakes. During the solidification, Mn and S should attain the supersaturation state, to nucleate MnS homogeneously, just before eutectic reaction after the oxides are nucleated in the interdendritic region as a result of microsegregation. Nucleation of MnS in the melt depends on the solubility product of Mn and S for the same amount of Mn or sulfur (one at a time) and does not depend on the Mn/S ratio.

(Mo,Cr)S seems to have nucleated graphite and then continued to grow along the graphite flake, resulting in small graphite branches. (Mo,Cr)S favors the formation of Mo_2C , which has an adverse effect on graphite precipitation if the amount exceeds a certain limit. The influence that Mo has together with Cr on graphite nucleation and growth morphology as well as the manner in which Mo affects MnS nucleation and the

lattice structure need to be investigated further. Thermodynamic analyses, whereby one considers the combination of different oxides with sulfides while creating complex compounds, are required for predicting oxide formation.

ACKNOWLEDGMENTS

The authors would like to thank Dr. Lena Magnusson for initiating the collaboration. Financial support provided by ELKEM-Norway is gratefully acknowledged.

APPENDICES

In all calculations, the concentration values are reported in wt pct, temperature in Kelvin, and ΔG in J/mol. The activities of SiO_2 , Al_2O_3 , CaO , CaS , SrO , SrS , MnS , and MoS_2 are assumed to be equal to one.

Appendix A: SiO_2

The oxygen concentration in the melt is determined by assuming thermodynamic equilibrium between Si and SiO_2 using the reaction $\text{Si}_l + 2[\text{O}]_l \leftrightarrow \text{SiO}_{2(s)}$. Considering activity, $a_{M/O} = C_{M/O} * f_{M/O}^{\text{melt}}$.^[27]

$$C_{\text{Si}} \cdot C_{\text{O}}^2 = \left(\frac{1}{f_{\text{Si}} \cdot f_{\text{O}}^2} \right) \cdot \exp\left(\frac{-\Delta G^o}{RT}\right) \quad [\text{A1}]$$

$$\Delta G^o = -(14200 - 55T)^{[27]} \quad [\text{A2}]$$

$$f_{\text{Si}} = 10^{0.24C_{\text{C}} + 0.093C_{\text{N}} + 0.086C_{\text{P}} + 0.057C_{\text{S}} + 0.32C_{\text{Si}}} = 27.08^{[27]}$$

$$f_{\text{O}} = 10^{-0.13C_{\text{C}} - 0.04C_{\text{Cr}} - 0.009C_{\text{Mn}} + 0.057C_{\text{N}} + 0.071C_{\text{P}} - 0.019C_{\text{S}} - 0.14C_{\text{Si}} - 0.94C_{\text{Al}}} = 0.1864$$

Appendix B: Al_2O_3

The reference state for the calculation is an infinitely dilute solution of oxygen in pure liquid iron. The reaction is $2\text{Al}_s + 3[\text{O}]_l \leftrightarrow \text{Al}_2\text{O}_{3(s)}$.^[27]

$$C_{\text{Al}}^2 \cdot C_{\text{O}}^3 = \left(\frac{1}{f_{\text{Al}}^2 \cdot f_{\text{O}}^3} \right) \cdot \exp\left(\left(-\frac{137158}{T}\right) + 42.254\right) \quad [\text{B1}]$$

$$f_{\text{Al}} = 10^{0.11C_{\text{C}} - 1.6C_{\text{O}} + 0.049C_{\text{S}} + 0.06C_{\text{Si}}} = 3.12$$

Appendix C: SrO

The Gibbs energy for SrO formation is calculated using Eq. [C1].^[28] Values for entropy, enthalpy, and heat capacity are taken from Kubaschewski *et al.*^[29] with the

exception of C_p^{SrO} ,^[30] which represents a solid-phase heat capacity. The interaction coefficients of Sr to other metals are unknown.

$$\Delta G^o = \Delta H_{298}^o + \int_{298}^T \Delta C_p dT - T \Delta S_{298}^o - T \int_{298}^T \left(\frac{\Delta C_p}{T} \right) dT \quad [\text{C1}]$$

$$\Delta G_{\text{SrO}} = 4.1868 \times [-1.358 \times 10^5 - 82.956T + 0.00414T^2 + (1.97 \times 10^{-7}T^3) + 17.64T \ln(T)] \quad [\text{C2}]$$

Appendix D: CaO

The free energy of formation of CaO is calculated from Eq. [C1] in two steps. The free energy for the phase changes that occur in Ca at 737 K and 1123 K (464 °C and 850 °C) is calculated as

$$\Delta G_{\text{Ca}} = 8686.7 - 14.75T + 0.01T^2 - 1.7 \times 10^{-6}T^3 \quad [\text{D1}]$$

The total free energy of formation of CaO is given in Eq. [D2].

$$\Delta G_{\text{CaO}} = 4.1858(-142981.6 + 20.9T + 0.0095T^2 - 1.42 \times 10^{-6}T^3 + 0.52T \ln(T)) \quad [\text{D2}]$$

The interaction coefficients for Ca with O and S are unknown.

Appendix E: CaS

The free energy of CaS formation is calculated using Eq. [C1] by considering the phase changes in S and Ca at different temperatures. The total free energy of S while cooling results in the formation of a monoatomic gas phase initially, followed by a liquid phase and then a solid phase as given by Eq. [E1].

$$\Delta G_{\text{S}} = -8772.44 + 6.95T + 0.0077T^2 - 1.4 \times 10^{-6}T^3 \quad [\text{E1}]$$

The total free energy of CaS formation is given in Eq. [E2], by substituting ΔG_{Ca} from Eq. [D1].

$$\Delta G_{\text{CaS}} = -130673.7 + 11.32T - 0.0038T^2 + 2.24T \ln(T) + 3 \times 10^{-7}T^3 \quad [\text{E2}]$$

Appendix F: MnS

Free energy of formation of MnS particles in the melt is given by Eq. [F1].^[27]

$$\Delta G_{\text{MnS}} = -266212 + 150.403T, \quad [27] \quad [\text{F1}]$$

$$f_{\text{Mn}} = 10^{C_N \cdot 0.078 + C_S \cdot 0.043} = 0.995 \quad [27]$$

$$f_s = 10^{0.24C_C - 0.022C_{Cr} - 0.012C_{Cu} - 0.025C_{Mn} - 0.028C_S + 1.87C_{Si}} \\ = 8.1 \quad [27]$$

Appendix G: MoS₂

Free energy of formation of MoS₂ is calculated using Eq. [C1]. The free energy for the phase changes in sulfur is given in Eq. [E1]. All of the data for MoS₂ are taken from the Smithells Metals reference book,^[31] except for $C_p^{\text{MoS}_2}$,^[30] which is the solid-phase heat capacity.

$$\Delta G_{\text{MoS}_2} = -\frac{1 \times 10^{-23}}{T} \\ \times \left(\begin{aligned} &1.599 \times 10^{28} T - 6.079 \times 10^{25} T^2 + 1.6484 \times 10^{21} T^3 \\ &- 1.5768 \times 10^{17} T^4 - 8.833 \times 10^8 T^5 - 4.81 \times 10^{28} \\ &+ 6.7834 \times 10^{24} \ln(T) T^2 \end{aligned} \right) \quad [\text{G1}]$$

$$f_{\text{Mo}} = 10^{0.021C_O - 0.07C_C - 0.078C_N} = 0.572 \quad (\text{from Appendix F}).$$

Appendix H: SrS

The free energy of formation of SrS is calculated using Eq. [H1].

$$\Delta G_{\text{SrS}} = \Delta G_{\text{S}(g \rightarrow l)} + \Delta G_{\text{S}(l \rightarrow s)} + \Delta G_{\text{Sr}(l \rightarrow s)} + RT \ln kp \quad [\text{H1}]$$

$$\Delta G_{\text{S}(g \rightarrow l)} = \frac{\Delta H_{\text{S}(gl)}(T - T_g)}{T_g} \quad [\text{H2}]$$

$$\Delta G_{\text{S}(l \rightarrow s)} = \frac{\Delta H_{\text{S}(ls)}(T - T_s)}{T_s} \quad [\text{H3}]$$

$$(\Delta G_{\text{Sr}(l \rightarrow s)}) = \frac{\Delta H_{\text{Sr}(ls)}(T - T_m)}{T_m} \quad [\text{H4}]$$

By substituting values from Elliott *et al.*^[32] and Smithells^[31] into Eq. [H1], we obtain the total Gibbs free energy given in Eq. [H5].

$$\Delta G_{\text{SrS}} = 66226.83 - 240.02T - 2.3 \times 10^{-5}T + 0.12716T^2 \quad [\text{H5}]$$

Appendix I: Supersaturation Models During Solidification

The minimum energy required to nucleate a particle is given as^[33]

$$\Delta G_a = 60.K_B.T = \left(\frac{16\pi}{3} \right) \frac{\sigma^3 (V_m^{M_x N_y})^2}{-\Delta G_n^2} \quad [33] \quad [\text{I1}]$$

The difference in the interaction coefficient on both sides is small and can therefore be neglected. Thus, we obtain the required equation for the supersaturation of particles that nucleate in the liquid between the dendrite arms as Eq. [I2].^[33]

$$C_M^X C_N^Y = (C_M^X C_N^Y)_{eq} \\ \times \exp \left[\left(\sqrt{\left(16\pi\sigma^3 (V_m^{M_x N_y})^2 \right) / (3k_B 60T)} \right) / RT \right] \quad [\text{I2}]$$

Scheil's equation is used for the segregation of Mn, Al, and Sr, while lever rule is used for the segregation of sulfur and oxygen^[34] and to calculate the supersaturation of oxide/sulfide as a function of the solid fraction. Equation [I3] is for microsegregation prior to eutectic reaction, while Eq. [I4] is used after eutectic reaction.

$$C_M^X C_N^Y = (C_M^o)^X (C_N^o)^Y \\ \times \left[(1 - f_\gamma)^{-\left(1 - k_M^z\right)} \right]^X / \left[1 - f_\gamma (1 - k_N^z) \right]^Y \quad [\text{I3}]$$

$$C_M^X C_N^Y = (C_M^o)^X (C_N^o)^Y \\ * \frac{\left[(1 - f_{\gamma+gr})^{-\left[(1 - k_M^{\gamma/l})f^\gamma + (1 - k_{gr}^L)f^{\gamma'}\right]} \right]^X}{\left[1 - f_{\gamma+gr} \left[(1 - k_N^{\gamma/l})f^\gamma + (1 - k_{gr}^L)f^{\gamma'} \right] \right]^Y} \quad (\text{I4})$$

Molar volumes are $V_m^{M_x N_y} = 21.8 * 10^{-6}$ (MnS); $20.3 * 10^{-6}$ (SrO); $34.33 * 10^{-6}$ (Al₂O₃). Partition coefficient are $k_O^{\gamma} = 0.054$ ^[33] $k_{Si}^{\gamma} = 1.3$ ^[35]; $k_{\text{graphite}}^l = 0.48$ ^[35]; $k_{Sr}^{\gamma} = 0.031$ ^[36]; $k_{Ce}^{\gamma} \cong k_{Ca}^{\gamma} = 0.063$ ^[36]; $k_{Al}^{\gamma} = 0.9$ ^[37]; $k_S^{\gamma} = 0.05$ ^[37]; $k_{Mn}^{\gamma} = 0.6$ ^[35]; $f_{\text{primary}}^{\gamma} = \frac{(3.709 - 3.4)}{(3.709 - 1.687)} = 0.152$. The weight fraction of graphite at the eutectic point is $f_E^{\text{gr}} = \frac{\rho_\gamma}{\rho_{\text{gr}}} * \left(\frac{3.4 - 1.687}{100 - 1.687} \right) = 0.0624$, $f_{gr}^{\text{vol}} = 0.0624 * f_{\text{remaining liq.}} = 0.0528$; $f_{(1-\text{gr})}^{\text{vol}} = (1 - f_E^{\text{gr}}) * f_{\text{remaining liq.}} + f_{\text{primary}}^{\gamma} = 0.947$, $f_{\text{solidified}}^{\text{total}} = f_{gr}^{\text{vol}} + f_\gamma^{\text{vol}}$.

Notations Index

C = concentration in wt pct; $f_{M,O,S}$ = interaction co-efficient of metal atoms and oxygen or sulfur atom in the melt; T = temperature in kelvin; ΔH° = standard heat of formation in J mol⁻¹; ΔC_p = change in

heat capacity in $\text{J k}^{-1} \text{mol}^{-1}$; ΔS° = standard change in entropy in J k^{-1} ; $\ln kp$ = natural logarithm of the equilibrium constant from reference state. (*s*, *l*, *g*) = solid, liquid, and gas respectively; ΔG_a = activation energy in J mol^{-1} ; ΔG_n = driving force of nucleation; K_B = Boltzmann's constant in $\text{J k}^{-1} = 1.38\text{e-}23$; σ = surface tension in J m^{-2} ; V_M = molar volume of metal oxide or sulfide in $\text{m}^3 \text{mol}^{-1}$; $C_{M,N}$ = concentration of metal atoms or Oxygen/sulfur atoms in the liquid in wt pct; $C_{(M,N)}^0$ = initial concentration of metal atoms of oxygen/sulfur atoms in the liquid; $(C_{M,N})_{\text{eq}}$ = equilibrium concentration of metal atoms or other; $f_{\gamma,\text{gr,E}}$ = solid fraction of austenite or graphite or eutectic phase, respectively, in the volume; ρ = density Kg m^{-3} .

REFERENCES

1. R.J. Warrick: *AFS Trans.*, 1966, vol. 74, pp. 722–33.
2. K.M. Muzmudar and J.F. Wallace: *AFS Trans.*, 1972, vol. 80, pp. 317–28.
3. K.M. Muzmudar and J.F. Wallace: *AFS Trans.*, 1973, vol. 81, pp. 412–23.
4. M.H. Jacobs, T.J. Law, D.A. Melford, and M.J. Stowell: *Met. Technol.*, 1974, vol. 1, p. 490–500.
5. M.A. Gadd and H.H.J. Bennett: *3rd International Symposium on the Physical Metallurgy of Cast Iron*, Elsevier, Stockholm, 1984, p. 99.
6. T. Kusakawa, S. Okimoto, K. Koayashi, Kazoo IDE, and H. Okita: Report of the Casting Research Laboratory, Waseda University, n. 39, 1988, pp. 25–32.
7. J. Campbell: *Metall. Mater. Trans. B*, 2009, vol. 40B, pp. 786–801.
8. I. Riposan, M. Chisamera, S. Stan, and D. White: *Int. J. Cast Met. Res.*, 2007, vol. 20, pp. 90–7.
9. I. Riposan, M. Chisamera, S. Stan, and T. Skaland: *Int. J. Cast Met. Res.*, 2003, vol. 16 (1–3), pp. 105–11.
10. I. Riposan, M. Chisamera, S. Stan, and D. White: *China Foundry*, 2009, vol. 6 (4), pp. 352–57.
11. I. Riposan, M. Chisamera, S. Stan, C. Hartung, and D. White: *Mater. Sci. Technol.*, 2010, vol. 26 (12), pp. 1439–47.
12. I. Riposan, M. Chisamera, S. Stan, E. Stefan, and C. Hartung: *Key Eng. Mater.*, 2011, vol. 457, pp. 19–24.
13. A. Velichko and F. Mücklich: *Int. J. Mater. Res.*, 2009, vol. 100 (8), pp. 1031–37.
14. T. Skaland: Ph.D. Thesis, Metallurgisk Institutt, Trondheim, Norway, 1992.
15. H. Gu and L. Weidong: *Adv. Mater. Res.*, 2011, vols. 299–300, pp. 576–79.
16. A. Sommerfeld and B. Tonn: *J. Mater. Sci. Technol.*, 2008, vol. 24 (3), pp. 321–24.
17. G.M. Goodrich, T.G. Oakwood and R.B. Gundlach: *AFS Trans.*, 2003, pp. 783–12.
18. E. Fraš and M. Górny: *Key Eng. Mater.*, 2011, vol. 457, pp. 137–42.
19. C.H. Wang and H. Fredriksson: *48th International Foundry Congress.*, Varna, 1981, p. 16.
20. J. Ekengård and A. Diószegi: *Proceedings of the Carl Loper Cast Iron Symposium*, Madison, Washington, 2009.
21. F. Lietaert: *Giessereiforschung*, 1997, vol. 3, pp. 106–23.
22. E.B. Ten: *Key Eng. Mater.*, 2011, vol. 457, pp. 43–47.
23. E. Fraš, H.F. López, and C. Podrzucki: *Int. J. Cast Metal Res.*, 2000, vol. 13, pp. 107–21.
24. A.D. Sy: *AFS Trans.*, 1967, vol. 75, pp. 161–72.
25. A. Roula and G.A. Kosnikov: *Mater. Lett.*, 2008, vol. 62, pp. 3796–99.
26. L. Magnusson: Ph.D. Thesis, Royal Institute of Technology, Stockholm, Sweden, 2006.
27. J.F. Elliott, M. Gleiser, and V. Ramakrishna: *Thermochemistry for Steelmaking*, Addison-Wesley, London, 1963, vol. 2, pp. 547–67.
28. O. Kubaschewski and C. B. Alcock: *Metallurgical Thermochemistry*, 5th ed., Pergamon Press Ltd., England, 1979, p. 19.
29. O. Kubaschewski and C. B. Alcock: *Metallurgical Thermochemistry*, 5th ed., Pergamon Press Ltd., England, 1979, p. 274–384.
30. M.W. Chase, Jr.: *NIST-JANAF Thermochemical Tables*, 4th ed., J. Phys. Chem. Ref. Data, Monograph 9, 1998, p. 1-1951.
31. E.A. Brandes and G.B. Brook: *Smithells Metals Reference Book*, 7th ed., Butterworth-Heinemann Ltd., Oxford, England, 1992, p. 8/1–8/51.
32. J.F. Elliott and M. Gleiser: *Thermochemistry for Steelmaking*, vol. 1, Addison-Wesley, London, 1960, p. 31–105.
33. H. Fredriksson and U. Åkerlind: *Materials Processing During Casting*, John Wiley, England, 2005, pp. 280–91.
34. H. Fredriksson and U. Åkerlind: Material: Royal Institute of Technology, Stockholm, Sweden, *Crystallization Processing*, vol. 2, unpublished research, 2011, p. 77.
35. A. Kagawa, K. Lwata, A.A. Nofal, and T. Okamoto: *Mater. Sci. Technol.*, 1985, vol. 1, pp. 678–83.
36. G.A. Jenner, S.F. Foley, S.E. Jackson, T.H. Green, B.J. Fryer, and H.P. Longerich: *Geochemica et Cosmochemica Acta*, 1994, vol. 58, pp. 5099–5103.
37. T.P. Battle and R.D. Pehlke: *Metall. Trans. B*, 1989, vol. 20B, pp. 149–60.